

pubs.acs.org/Biomac Article

Virus-Like Particles (VLPs) as a Platform for Hierarchical Compartmentalization

Hitesh Kumar Waghwani, Masaki Uchida, Chi-Yu Fu, Benjamin LaFrance, Jhanvi Sharma, Kimberly McCoy, and Trevor Douglas*



Cite This: *Biomacromolecules* 2020, 21, 2060–2072



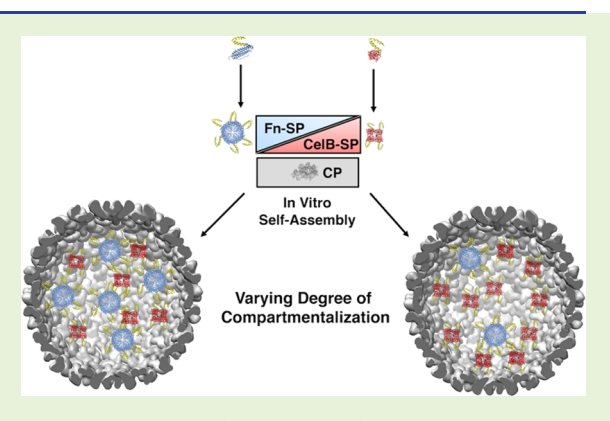
ACCESS

Metrics & More

Article Recommendations

Supporting Information

ABSTRACT: Hierarchically self-assembled structures are common in biology, but it is often challenging to design and fabricate synthetic analogs. The archetypal cell is defined by hierarchically organized multicompartmentalized structures with boundaries that delineate the interior from exterior environments and is an inspiration for complex functional materials. Here, we have demonstrated an approach to the design and construction of a nested protein cage system that can additionally incorporate the packing of other functional macromolecules and exhibit some of the features of a minimal synthetic cell-like material. We have demonstrated a strategy for controlled co-packaging of subcompartments, ferritin (Fn) cages, together with active cellobiose-hydrolyzing β -glycosidase enzyme macromolecules, CelB, inside the sequestered volume of the bacteriophage P22 capsid. Using controlled



in vitro assembly, we were able to modulate the stoichiometry of Fn cages and CelB encapsulated inside the P22 to control the degree of compartmentalization. The co-encapsulated enzyme CelB showed catalytic activity even when packaged at high total macromolecular concentrations comparable to an intracellular environment. This approach could be used as a model to create synthetic protein-based protocells that can confine smaller functionalized proto-organelles and additional macromolecules to support a range of biochemical reactions.

■ INTRODUCTION

Compartmentalization is one of the hallmarks of biological systems. The archetypal cell is defined by a boundary that delineates the interior from exterior environments.² The intracellular environment is highly concentrated with macromolecules, and in eukaryotic cells there are also well-defined lipid-based subcellular compartments with specialized functions.3 While prokaryotes lack lipid-based subcellular compartments, they do have many examples of protein-based compartments, which function similarly to isolate certain metabolic processes within the cell.⁴ An excellent example of these are bacterial microcompartments, such as the carboxysomes, in which enzymes are sequestered within a proteinaceous shell. These cage-like structures encapsulate multiple copies of the enzymes ribulose 1,5-bisphosphates carboxylase/ oxygenase (RuBisCO) and carbonic anhydrase and are central to carbon fixation.5

Synthetic approaches to the formation of hierarchical protein cage-based materials 6-10 and compartments able to carry out cell-like, or sub-cellular-like, behavior 3,11-16 are of interest for the development of new functional materials. Developing such materials requires control over the compartment size, the incorporation of multiple distinct macromolecules (with control over their stoichiometries and packing

density), the permeability, and the degree of compartmentalization, 16-21 where the degree of compartmentalization can be defined as the number of subcompartments present inside a larger compartment. Micro- to millimeter-sized multicompartment systems have been created *in vitro* using inorganic, 22 protein membranes, 23 or phase-separated liquid microdroplets, 4 polymers, 25-28 and lipids. 29-31 However, the limitations of such particles are size heterogeneity, 32-36 low encapsulation efficiency, 26,37 the need for harsh solvents for template removal, 38,39 limited control over the degree of compartmentalization, 29,40,41 and low molecular permeability. 42 Developing multicompartment particles with near molecular precision is complex and presents significant synthetic challenges, but overcoming these may allow us to mimic the complex cellular function in synthetic nanocompartments and is the current focus of this study. Inspiration for this work comes from the naturally occurring nested structures such as mamavirus, which

Received: January 8, 2020 Revised: April 21, 2020 Published: April 22, 2020





contains the sputnik virus inside the capsid, 43,44 and the functionally distinct icosahedral nanocompartment from *Thermotoga maritima* called encapsulin, which contains ferritin-like proteins (FLPs) or peroxidases involved in the mitigation of oxidative stress. 45–47

The previous work used the protein cage lumazine synthase as the larger cage (30 nm diameter) and exploited charge complementarity to form a nested structure where on average two ferritin (Fn) cages (12 nm diameter) were encapsulated. 15 Compartmentalization with the special organization of distinct functional components is the key feature of eukaryotic cells.^{1,3} Our goal in this research is to provide a proof-of-principle demonstration that we can emulate natural compartmentalization using a hierarchical protein-based system. Fn naturally catalyzes iron oxide mineralization⁴⁸ but has also been used as an artificial compartment for synthetic nanoparticles⁴⁹ and enzyme encapsulation. 50 Here, we demonstrate the fabrication of a nested "cage-within-a-cage" structure as a synthetic organelle mimic, with control over the density of subcompartments and the stoichiometric co-packaging of other active macromolecules. In our synthetic system, we have used the virus-like particle (VLP) derived from the P22 bacteriophage as a large permeable compartment (56 nm diameter), human ferritin (Fn) as a smaller cage, which defines subcompartments, and the cellobiose-hydrolyzing enzyme (CelB) as a catalytically active, co-encapsulated, macromolecule. Encapsulation of the small compartments and active macromolecules was directed through selective noncovalent interactions to the VLP during assembly and high-density packing of the cargos was obtained.

The P22 VLPs have previously been used as protein-based compartments for encapsulating a variety of cargo molecules, including proteins, peptides, polymers, and small organic molecules. 51-54 The P22 VLP self-assembles from 420 copies of the coat protein (CP) and a variable number of scaffold protein (SP) subunits (typically 100-300 copies) through noncovalent interactions to form a procapsid structure.5 Genetic fusion of a cargo protein to a truncated form of the SP (SP₁₄₁) maintains the ability to direct the capsid assembly and results in encapsulation of the SP-fused cargo inside the P22 during assembly. 57,58 Ferritin protein cages are encapsulated as cargos, which can themselves provide unique confined local volumes for cargo encapsulation (mineral and enzyme).^{49,50} In this study, we genetically fused the ferritin subunit to the SP₁₄₁ to direct encapsulation of multiple copies of ferritin cages inside P22 VLPs using both in vivo (assembly inside Escherichia coli) and in vitro (assembly in a test tube) self-assembly approaches. To further mimic a cell-like environment with multiple distinct macromolecules, we investigated the encapsulation of homotetrameric β -glycosidase enzyme CelB from Pyrococcus furiosus as additional co-packaged macromolecules within P22 VLPs. Intentionally, there is no biochemical connection between the encapsulation of these two cargos inside P22. We are demonstrating here that it is possible to co-encapsulate two very different types of protein macromolecules inside VLPs with control over their packing stoichiometry and also that multiple levels of hierarchical assembly are possible, by design. The in vitro approach allowed control over an additional level of complexity through the coencapsulation of Fn-SP cages and the enzyme CelB-SP within the P22 capsid with controlled encapsulation stoichiometry. These results indicate that both the degree of compartmentalization and the cargo stoichiometries could be readily tuned at the molecular level. The macromolecular concentrations

within the VLP are similar to the estimated cell-like macromolecular concentrations (\sim 300 mg mL⁻¹)⁵⁹ and the co-encapsulated CelB enzymes showed catalytic activity in the highly crowded environment within the VLP. Thus, we have established a design and synthetic strategy to produce a protein-based hierarchical self-assembly system that exhibits some of the structural and functional features of a synthetic cell.

■ EXPERIMENTAL SECTION

Materials. E. cloni EXPRESS BL21(DE3) Electrocompetent cells were purchased from Lucigen (Middleton, WI). Thrombin from bovine plasma, DNase, RNase, and lysozyme were purchased from Sigma-Aldrich (St. Louis, MO). All other chemicals and reagents were purchased from Thermo Fisher Scientific (Waltham, MA).

Plasmid Construction for Simultaneous Co-expression of Fn-SP and CP. A previously prepared pETDuet-1 vector containing the truncated scaffold protein SP₁₄₁ (residues 142–303 of P22 scaffolding protein) inserted into multiple cloning site 1 with BamHI/SacI and P22 coat protein (in multiple cloning site 2 with NdeI/XhoI) was used as a platform for vector construction. ⁵¹ The human heavy-chain ferritin (Fn) gene was amplified with OneTaq DNA polymerase (New England Biolabs; Ipswich, MA) from a previously prepared plasmid⁶⁰ using a forward primer containing a NcoI site and a reverse primer containing a BamHI site. Ligation of the Fn gene to SP141 in the pETDuet-1 vector was carried out by digestion of both Fn and the vector with NcoI and BamHI, followed by ligation using T4 DNA ligase (New England Biolabs). A ten amino acid linker (AGSLVPRGSC) including a thrombin recognition sequence was inserted between Fn and SP₁₄₁. Base pair and amino acid sequences of Fn-SP and CP are available in Supporting Information (SI), Sections 1 and 2.

Plasmid Construction for Sequential Expression of Fn-SP and CP. DNA sequences coding each protein were inserted into different vectors, i.e., the Fn-SP gene was inserted into the *NcoI/Hin*dIII site of the pBAD/His B vector (Invitrogen) and the CP gene was inserted into the *NdeI/Xho*I site in the multiple cloning site 2 of the pRSFDuet-1 vector (Novagen). This allowed sequential expression of Fn-SP followed by CP, which can be induced with arabinose and isopropyl β-D-thiogalactopyranoside (IPTG), respectively, in an *E. coli* expression system.

Plasmid Construction for CelB-SP₁₄₁6xHis (CelB-SP). A variant pBAD vector that will produce CelB-SP₁₄₁ with a C-terminal His-tag was engineered by amplifying previously prepared vector encoding for CelB-SP₁₄₁⁵¹ by polymerase chain reaction (PCR) using forward primer 5′- GAT ATA CCA TGG CAA AGT TCC CAA AAA ACT TCA TGT TTG G -3′ and reverse primer 5′- GCA TGA GCT CTT AAT GGT GAT GGT GAT GGT GAG ACA CTC GGA TTC CTT TAA GTT TTG CCT TTA GCT TGC -3′. The forward primer included the NcoI restriction site and the reverse primer included the SacI restriction site. The PCR product was purified, digested with NcoI and SacI restriction enzymes, and ligated into the pBAD vector that had been digested with the same enzymes and dephosphorylated. The identity of the ligated vector was determined by sequencing and histidine tag insertion was confirmed (sequence details is provided in Supporting Information, Sections 1 and 2).

Protein Expression. For simultaneous co-expression of Fn-SP and CP, the pETDuet-1 vector was transformed into BL21 (DE3) *E. coli* strain. The cells were seeded on a LB agar plate supplemented with 50 μ g mL⁻¹ ampicillin for selection and the plate was incubated at 37 °C overnight. A colony was picked and grown in the LB medium at 37 °C in the presence of ampicillin to maintain selection. Expression of Fn-SP and CP were concurrently induced by addition of IPTG to a final concentration of 0.3 mM when the optical density (o.d.) of the culture at 600 nm reached 0.6. The culture was grown for 4 h after addition of IPTG, the cells were harvested by centrifugation (4500g for 20 min), and cell pellets were stored at -80 °C until further purification of the protein.

For controlled sequential expression of Fn-SP and CP, a two-vector expression approach was used. The pRSFDuet-1 vector (kanamycin resistance) with CP (but no SP) and the pBAD vector (ampicillin resistance) with Fn-SP were co-transformed into BL21 (DE3) E. coli cells. The cells were plated on a LB agar plate supplemented with 50 μg mL⁻¹ ampicillin and 30 μg mL⁻¹ kanamycin to select *E. coli* colonies with both vectors, and the plate was incubated at 37 °C overnight. One colony was picked and grown in the LB medium at 37 °C in the presence of ampicillin and kanamycin to maintain selection for both plasmids. The expression of Fn-SP was induced by the addition of L-arabinose to a final concentration of 13.3 mM when the o.d. at 600 nm reached 0.6. After Fn-SP was expressed for 4 h, expression of the CP was induced with IPTG to a final concentration of 0.3 mM and the culture was grown for an additional 3 h. Cells were harvested by centrifugation (4500g for 20 min), and cell pellets were stored at -80 °C until further use.

For expression of Fn-SP alone, the pETDuet-1 vector containing the Fn-SP gene alone was transformed into *E. coli* BL21 (DE3) strain. The cells were seeded on a LB agar plate supplemented with ampicillin antibiotic (50 μg mL⁻¹) for selection and the plate was incubated at 37 °C overnight. A colony was picked and grown in the LB medium at 37 °C in the presence of ampicillin (50 μg mL⁻¹). Expression of Fn-SP was induced by addition of IPTG to a final concentration of 0.3 mM at o.d. of 0.6 at 600 nm. The culture was grown for 4 h after addition of IPTG, the cells were harvested by centrifugation (4500g for 20 min), and cell pellets were stored at -80 °C until further purification of the protein.

Expression and purification of P22S39C,⁵³ wtSP,⁵⁸ and wild-type human heavy-chain ferritin⁶¹ was done according to previously reported procedures.

Protein Purification. P22 VLPs were purified using the previously reported procedure⁵⁸ with slight modification. Briefly, cell pellets were resuspended in 50 mM sodium phosphate, 100 mM sodium chloride pH 7.0 buffer (hereafter referred as phosphate buffer). DNase, RNase, and lysozyme were added to final concentrations of 60, 100, and 50 $\mu g \text{ mL}^{-1}$, respectively. The cell suspension was incubated for 30 min at room temperature with gentle shaking. Cells were lysed by sonication for 2 min at 50% amplitude on ice. The cell debris was separated from the cell lysate by centrifugation (12 000g, 45 min, 4 °C) and the cell lysate was passed through a 0.45 μ m filter. VLPs were purified from the cell lysate by ultracentrifugation over a 35% (w/v) sucrose cushion at 45 000 rpm (F50L-8 × 39 rotor, Piramoon Technologies) for 50 min. The resulting VLPs were resuspended in phosphate buffer, spun on a benchtop centrifuge (13 000 rpm, 10 min) to remove any protein aggregates, and further purified over a Sephacryl S-500 HR size-exclusion column (GE Healthcare Life Sciences) using fast protein liquid chromatography (FPLC) (Bio-Logic DuoFlow, BioRad, Hercules, CA) at the 1 mL min⁻¹ flow rate of phosphate buffer. Fractions containing P22 VLPs were concentrated by ultracentrifugation at 45 000 rpm for 50 min, and the resulting pellets were resuspended in phosphate buffer.

The Fn-SP cell pellet was lysed using a similar procedure as described above with slight modification. The cell lysate collected after centrifugation was heated at 40 °C (to remove other heat labile proteins from E. coli) and the resultant aggregates were removed from the cell lysate by centrifugation (12 000g, 30 min, 4 °C). The resulting soluble protein was dialyzed in 50 mM sodium phosphate, 1 M sodium chloride pH 7.0 buffer for 4 h, filtered by 0.2 μ m filter before purifying over a Superose 6 prep grade size-exclusion column (GE Healthcare Life Sciences) using FPLC at the 0.5 mL min⁻¹ flow rate of phosphate buffer. Purified protein was analyzed by sodium dodecyl sulfate polyacrylamide gel electrophoresis (SDS-PAGE) and fractions containing Fn-SP protein were further purified by a Mono S cation exchange chromatography column (GE Healthcare) using 20 mM sodium phosphate buffer pH 7.0 with the 0-1 M sodium chloride gradient. Fractions containing purified Fn-SP protein were combined and stored at 4 °C.

Morphological Transformation of P22-Fn Procapsid. The morphological transformation of P22-Fn from procapsid (PC) to expanded form (EX) by heat treatment was achieved as previously

described. ⁶² Briefly, purified P22-Fn VLP ($500 \mu L$, 3 mg mL⁻¹) was heated at 70 °C for 20 min. The heat-treated samples were purified by ultracentrifugation ($45\,000$ rpm, 50 min) and further analyzed with native agarose gel where EX samples migrate slower than PC.

To assess the stability of P22-Fn-nested cages, 1 mL of P22-Fn PC VLPs (1 mg mL $^{-1}$) was heated at 75 °C for 20 min to form P22-Fn Wiffle ball (WB) VLPs and cooled back to room temperature. The heated P22-Fn VLPs were further centrifuged at 14 000 rpm for 10 min to remove any protein aggregates followed by ultracentrifugation. VLPs were resuspended in 50 mM sodium phosphate 100 mM NaCl pH 7 buffer until further use.

P22-Fn in Vitro Assembly. P22S39C ES particles were prepared using the previously reported procedure (Figures S13 and 14).51 P22S39C ES VLPs were buffer-exchanged to 50 mM Tris-HCl, 25 mM sodium chloride, 2 mM ethylenediaminetetraacetic acid (EDTA), 3 mM β -mercaptoethanol, and 1% glycerol pH 7.6 (hereafter referred as assembly buffer) using a 100 kDa Amicon ultra-15 centrifugal filter. Twelve mL ES VLP sample (in phosphate buffer) was concentrated by centrifugation (5000g, 10 min) in Amicon ultra-15, the filtrate was discarded, and the concentrate was reconstituted to the original sample volume with assembly buffer. This process was repeated at least 3 times for thorough buffer exchange. ES particles were then disassembled into individual CP subunits as previously described. 58,63,64 Briefly, ES particles were mixed with 6 M GuHCl in assembly buffer (1:1 volume ratio) to a final GuHCl concentration of 3 M, followed by incubation for 1.5 h at room temperature with gentle shaking. The protein solution was centrifuged at 13 000 rpm for 10 min to remove any protein aggregates, and the concentration of CP subunits was determined by absorbance at 280 nm (extinction coefficient of 0.963 (mg mL) $^{-1}$ cm $^{-1}$) 65,66 and adjusted to prepare 0.8 mg mL $^{-1}$ protein solution.

Purified Fn-SP cages were buffer-exchanged into assembly buffer using a 100 kDa Amicon ultra-15 centrifugal filter as described above. The protein solution was centrifuged at 13 000 rpm for 10 min to remove any protein aggregates, passed through a 0.22 μ m syringe filter and the protein concentration was determined by absorbance at 280 nm (extinction coefficient of 0.7 (mg mL)⁻¹·cm⁻¹) and adjusted to 0.24, 0.48, and 0.68 mg mL⁻¹.

Denatured CP subunits and the Fn-SP cage were mixed for P22-Fn assembly in the following manner: CP subunits in 3 M GuHCl in assembly buffer were mixed in an equal volume with Fn-SP (varied Fn-SP/CP ratios by varying Fn-SP concentration) in assembly buffer. Fn-SP to CP at the subunit molar ratio of 0.55:1, 1.1:1, and 1.6:1 was tested at a constant 0.8 mg mL⁻¹ concentration of CP. As a control experiment, CP subunits were mixed with wtSP (Figure S2). The concentration of GuHCl in all reaction mixtures was 1.5 M. The reaction mixtures were immediately dialyzed into assembly buffer twice for a total of 12–18 h. The resulting assembled P22-Fn particles were spun down on the benchtop centrifuge (13 000 rpm, 10 min) to remove protein aggregates. P22-Fn particles were pelleted by ultracentrifugation (43 000 rpm for 50 min, F50L-24 × 1.5 rotor, Thermo Scientific), followed by resuspension in phosphate buffer.

Co-encapsulation of Fn-SP and CelB-SP in P22 through in Vitro Assembly. Co-encapsulation of Fn-SP and CelB-SP in P22 VLPs was performed using the in vitro assembly method described above with a slight modification. Purified Fn-SP and CelB-SP proteins (Figures S1 and S12) were buffer-exchanged into the assembly buffer. To assemble P22 VLPs with both Fn-SP cages and CelB-SP proteins, CP subunits in 3 M GuHCl in assembly buffer were mixed with an equal volume of a mixture of Fn-SP and CelB-SP. The volume ratio of Fn-SP and CelB-SP was adjusted to obtain Fn-SP to CelB-SP subunit molar ratios of 1:1, 1:3, and 1:6. In all co-assembly experiments, the SP_(total)/CP ratio was kept at 1.6:1.⁶³ Single-cargo encapsulation of either Fn-SP or CelB-SP was performed as controls. The reaction mixtures were dialyzed in assembly buffer twice for a total of 12-18 h to induce VLP formation. The resulting co-assembled P22-Fn-CelB particles were purified by ultracentrifugation (43 000 rpm for 50 min), followed by resuspension in phosphate buffer.

Thrombin Digestion and Iron Oxide Mineralization in Fn and P22 VLP Variants. Purified Fn-SP cages were buffer-exchanged into

50 mM sodium bicarbonate 100 mM NaCl pH 9 by dialysis (×2). Fn-SP cages (6 mL, 1 mg mL $^{-1}$) were incubated with 200 unit of thrombin protease at 37 $^{\circ}$ C overnight, which resulted in the formation of Fn-linker cages (22 kDa, subunit $M_{\rm w}$) and linker-SP (18.1 kDa) as cleavage products that were separated using size-exclusion chromatography. Under similar experimental conditions, thrombin digestion of P22-Fn WB VLPs (1.2 mL, 1 mg mL $^{-1}$) was carried out with 200 units, and thrombin-treated VLPs were purified by ultracentrifugation (×2).

Each protein sample (1 mL, 0.25 mg mL^{-1} in 100 mM MES, 100 mM sodium chloride pH 6.5) was taken into a separate vial. Ammonium iron(II) sulfate hexahydrate $(NH_4)_2Fe(SO_4)\cdot(6H_2O)$ and atmospheric oxygen were used as the iron source and oxidant, respectively. The iron oxide mineralization capability of Fn-cage variants (Fn-SP, Fn-linker, Fn control) was tested under total loading of 2000 Fe²⁺ per cage and P22 VLP variants P22-Fn WB and P22-Fn WB (thrombin) under total loading of 21 600 Fe²⁺ per VLP. A protein-free sample was also used as a control. To achieve a theoretical iron loading factor of 2000 Fe per Fn-cage variant, 9.8, 9.5, and 5.2 μ L of 10 mM Fe²⁺ stock solution were added to Fn, Fn-linker, and Fn-SP protein solution, respectively, every 20 min (corresponding to addition of 200 Fe²⁺ per increment). Similarly, to achieve a theoretical iron loading factor of 21 600 Fe per P22 VLP variant, 2.1 and 2.6 μ L of 10 mM Fe²⁺ stock solution were added every 20 min (corresponding to addition of 2400 Fe²⁺ per increment). The iron oxide mineralization reaction was monitored by UV-vis spectroscopy at 420 nm (iron oxide mineral formation) and 800 nm (scattering due to formation of bulk precipitates).

Size-Exclusion Chromatography Coupled With Multiangle Light Scattering (SEC-MALS). The molecular weights, hydrodynamic radius (R_h) , and radius of gyration (R_g) for samples were analyzed by multiangle light scattering (MALS:DAWN8+, Wyatt Technology, Santa Barbara, CA) equipped with a He-Ne laser source, quasi-elastic light scattering detector, and refractive index (RI) detector (Optilab T-rEX, Wyatt Technology), which is coupled with an Agilent 1200 HPLC system. All P22 variant samples were separated over a WTC-0200S (Wyatt technologies) size-exclusion column at the flow rate of 0.7 mL min⁻¹ of MALS buffer (50 mM sodium phosphate, 100 mM sodium chloride, 200 ppm sodium azide pH 7.2). A 25 μ L sample was injected and loaded on a column. The eluted protein peaks were detected using a UV-vis detector (Agilent), a Wyatt HELEOS multiangle laser light scattering (MALS) detector, and an Optilab rEX differential refractometer. The number-average particle molecular weight was measured across each protein peak using Astra 6.0.3.16 software (Wyatt Technologies Corporation). A refractive index increment (dn/dc) of protein (0.185) was used to calculate the molecular weight of the samples. The average molecular weight (M_w) contribution from cargo was determined by subtracting $M_{\rm w}$ of P22 ES (19.6 MDa) from cargo-filled P22 VLP samples. A similar procedure was used to determine M_w contribution from two cargoes in the coassembled samples.

SDS-PAGE Gel Electrophoresis. Protein samples were mixed with the 4× SDS-PAGE loading buffer (containing 100 mM DTT final concentration) and heated in a boiling water bath for 10 min. Samples were spun on a benchtop centrifuge and separated on a 12% acrylamide gel at a constant current of 36 mA for approximately 1 h. Gels were stained with InstantBlue protein stain (Expedeon) and rinsed with water before imaging. The gel image was recorded on a UVP MultiDoc-IT digital imaging system. A 10–180 kDa PageRuler prestained protein ladder (Thermo Scientific) was used as a protein marker.

Densitometry. Densitometry analysis of SDS-PAGE gel was used to determine the relative subunit ratio of Fn-SP and CelB-SP to CP in the co-encapsulation reaction using the previously described method with slight modification. A sample calculation to estimate $M_{\rm w}$ contribution from Fn-SP and CelB-SP per capsid in the coencapsulated VLP is shown in Supporting Information, Section 12. Briefly, 10 μ L protein samples were applied and separated on a 12% SDS-PAGE gel (Figure 5b). The line scan profiles of CP, Fn-SP, and CelB-SP protein bands were obtained using Fiji software and fitted

with multipeak Gaussian fit function using Igor Pro 6.37 to obtain peak areas (Figure S15). Peak areas of Fn-SP, CelB-SP were normalized to constant CP concentrations. The peak area ratio of Fn-SP to total cargo peak area (Fn-SP+CelB-SP) was taken into consideration and inferred in total cargo $M_{\rm w}$ (Fn-SP+CelB-SP) obtained from SEC-MALS to estimate average $M_{\rm w}$ contribution by Fn-SP in the P22-Fn-CelB co-encapsulation sample. A similar calculation was done for determining $M_{\rm w}$ contribution by CelB-SP in the co-assembled sample.

Transmission Electron Microscopy (TEM). Protein samples (5 μ L, 0.2–0.3 mg mL⁻¹) were applied to 400 mesh carbon-coated copper grids and incubated for 2 min. Excess liquid was wicked away with a filter paper. The sample grid was then washed with 5 μ L of distilled water to remove salts and stained with 5 μ L of 2% uranyl acetate for 2 min. Excess stain was wicked away using the filter paper. Images were taken on a JEOL 1010 transmission electron microscope at an accelerating voltage of 80 kV. The particle size (diameter) of protein cage nanoparticles in the TEM images was measured using Fiji software ⁶⁷ to generate size distributions. The scale bar in the inset TEM image was inserted with Fiji software ⁶⁷ using the scale bar from the stage micrometer as standard. The contrast of TEM images was enhanced in Fiji for clarity.

Dynamic Light Scattering (DLS). The hydrodynamic radius ($R_{\rm h}$) of protein samples was measured by dynamic light scattering (DLS) (Zetasizer Nano-S; Malvern Instruments, Worcestershire, U.K.). Protein samples were spun in a benchtop centrifuge (12 000 rpm, 10 min) to remove any aggregates. The DLS of each sample (100 μ L, 1 mg mL⁻¹) was measured in a quartz cuvette (Hellma Analytics, ZEN2112).

Cryo-Electron Tomography. P22-Fn VLPs were mixed with 10 nm gold colloidal beads and applied to plasma-cleaned holey carbon grids (Quantifoil Copper R2/2 grids, 300 mesh). The grids were plungefrozen in liquid ethane using a Vitrobot (FEI Inc.) and stored in liquid nitrogen. The specimens were imaged using an FEI Tecnai TF20 Twin transmission electron microscope at an accelerating voltage of 200 kV. Tilt series covering an angular range from -60° to $+60^{\circ}$ with 1° increment were acquired automatically using Leginon at approximately 5 nm underfocus with 120 electrons per Å² total dose. 68,69 Images were recorded with a Gatan 4K-by-4K-pixel chargecoupled device at 3.52 Å/pix on the specimen. Tilt series were aligned with gold fiducials and the tomograms were reconstructed with IMOD.⁷⁰ Subtomography volumes containing individual Fn cages were computationally selected from the cryo-ET reconstruction of P22-Fn VLPs. The crystal structure of ferritin (PDB: 2FHA)⁴⁸ was fit to the individual density of the Fn-SP cage using UCSF Chimera.

P22-Fn-CelB β -Glycosidase Kinetic Assay. Kinetics assays on CelB co-encapsulated with the Fn-SP cage in P22 were carried out in a similar way as described by Patterson et al.⁵¹ using P22-CelB as a control. Activity assays were carried out at 50 °C on an Agilent 8453 UV-vis spectrophotometer with a temperature control module. Buffers were preheated at 50 °C. Kinetics assays were carried out in 60 mM sodium citrate buffer, pH 7.0. One microliter of either P22-CelB or P22-Fn-CelB (concentrations adjusted according to the CelB monomer as 1 µM) was added to preheated cuvettes containing 99 μ L of 4-nitrophenyl- β -glucopyranoside (PNPG, 0.1–3 mM) in citrate buffer to give a total reaction volume of 100 μ L and the solution was mixed thoroughly by pipetting. The appearance of 4-nitrophenol was monitored by the increase in the absorbance at 405 nm (extinction coefficient of 9.44 M⁻¹ cm⁻¹ in citrate buffer was used as previously reported).⁵¹ The activity assays were carried out in triplicate. Plots of the initial rates were corrected for any nonenzymatic degradation of 4nitrophenyl- β -glucopyranoside and were fit to the Michaelis-Menten kinetics model using Igor Pro 6.37.

■ RESULTS AND DISCUSSION

Ferritin-Scaffold Fusion Protein (Fn-SP). The gene encoding the human heavy-chain ferritin subunit (Fn) was fused to the 5' end of the truncated scaffold protein gene $(SP_{141}$, amino acids 142-303) to form Fn-SP (Figure 1a),

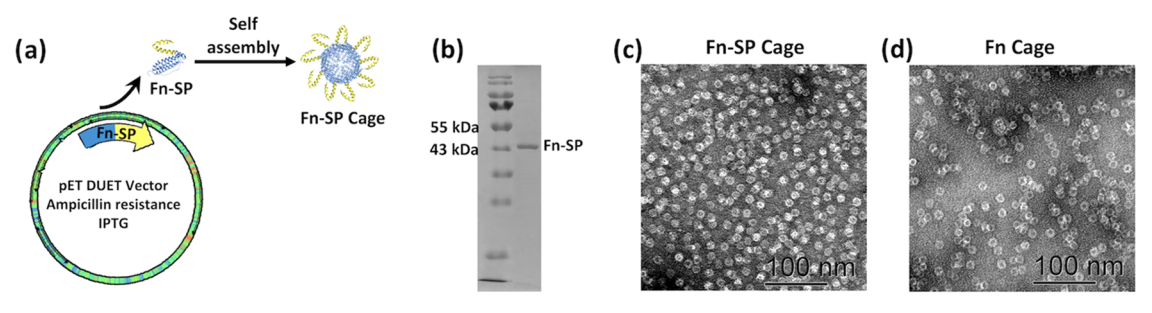


Figure 1. (a) Expression of recombinant ferritin-scaffold protein fusion (Fn-SP) results in self-assembly of the ferritin-like cage structure. (b) SDS-PAGE analysis of purified Fn-SP particles showed an \sim 40 kDa protein band corresponding to the Fn-SP subunit. TEM micrographs showing Fn-SP cages (c) 14.2 ± 0.5 nm, morphologically similar to Fn cages (d) 12.9 ± 0.5 nm.

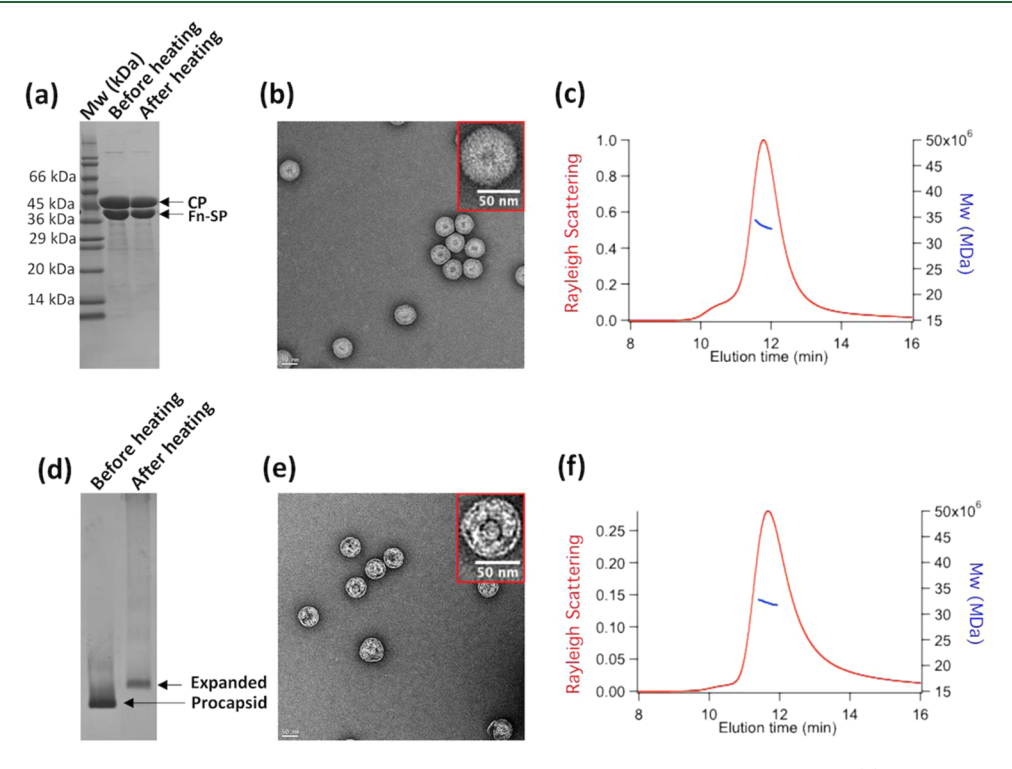


Figure 2. Characterization of P22-Fn VLPs self-assembled *in vivo* using the single-vector expression system. (a) SDS-PAGE analysis of P22-Fn VLPs showed CP and Fn-SP subunit bands before and after heat treatment. (b) TEM of P22-Fn PC VLPs (before heat treatment) showed 59.2 \pm 1.25 nm spherical protein cages with no clear Fn-cage-like density inside P22. (c) SEC-MALS analysis of P22-Fn PC VLPs showed the radius of gyration of 24.2 \pm 0.1 nm and molar mass of 33.44 \pm 0.09 MDa corresponding to encapsulation of ~340 Fn-SP subunits. (d) Native agarose gel electrophoresis, after heat treatment, confirmed the structural transition of P22-Fn from PC to EX. (e) TEM of P22-Fn EX VLPs showed 64.6 \pm 1.6 nm particles with some cage-like density of Fn inside P22. (f) Molar mass of P22-Fn EX VLPs by SEC-MALS was observed to be 32.36 \pm 0.21 MDa and the radius of gyration (R_g) as 25.6 \pm 0.05 nm.

which was subsequently expressed in *E. coli* and purified. Before testing encapsulation of Fn-SP inside the P22 VLPs, we first verified that the genetic fusion of the SP₁₄₁ did not disrupt the self-assembly of the Fn subunits into a cage-like quaternary structure. The purified Fn-SP protein (Figure S1) showed a 40 kDa band corresponding to the expected size of the Fn-SP subunit (Figure 1b) when characterized by sodium dodecyl sulfate polyacrylamide gel electrophoresis (SDS-PAGE). Transmission electron microscopy (TEM) showed the formation of the 14.2 ± 0.5 nm spherical protein cage (Figure 1c), which was indistinguishable from wild-type ferritin (Figure 1d). The hydrodynamic radius of Fn-SP cages, measured by dynamic light scattering, was 15 nm \pm 0.2 nm (Figure S1), which is larger than wild-type ferritin (12.2 ± 0.16 nm) due to the SP₁₄₁ fused to ferritin.

Simultaneous Co-expression of Fn-SP and CP in the E. coli Expression System. Simultaneous expression of both the Fn-SP and CP proteins in E. coli (BL21 DE3) resulted in the assembly of Fn encapsulated within P22 (P22-Fn) VLP. Analysis of the purified P22-Fn procapsid VLPs by SDS-PAGE showed bands corresponding to Fn-SP (40 kDa) and CP (46 kDa) (Figure 2a) subunits. The molecular weight of P22-Fn PC, determined by size-exclusion chromatography coupled to multiangle light scattering (SEC-MALS), was observed to be 33.44 ± 0.09 MDa (Figure 2c), which is ~13.8 MDa larger than P22 VLP without any cargo molecules inside. This indicates the successful encapsulation of ~340 Fn-SP subunits on average within the P22 VLP. TEM observation of the sample verified that the P22 VLPs had assembled into cage-like structures of diameter 59.2 \pm 1.25 nm (Figure 2b) that resembled the size and morphology of wtP22 VLP (Figure S2).

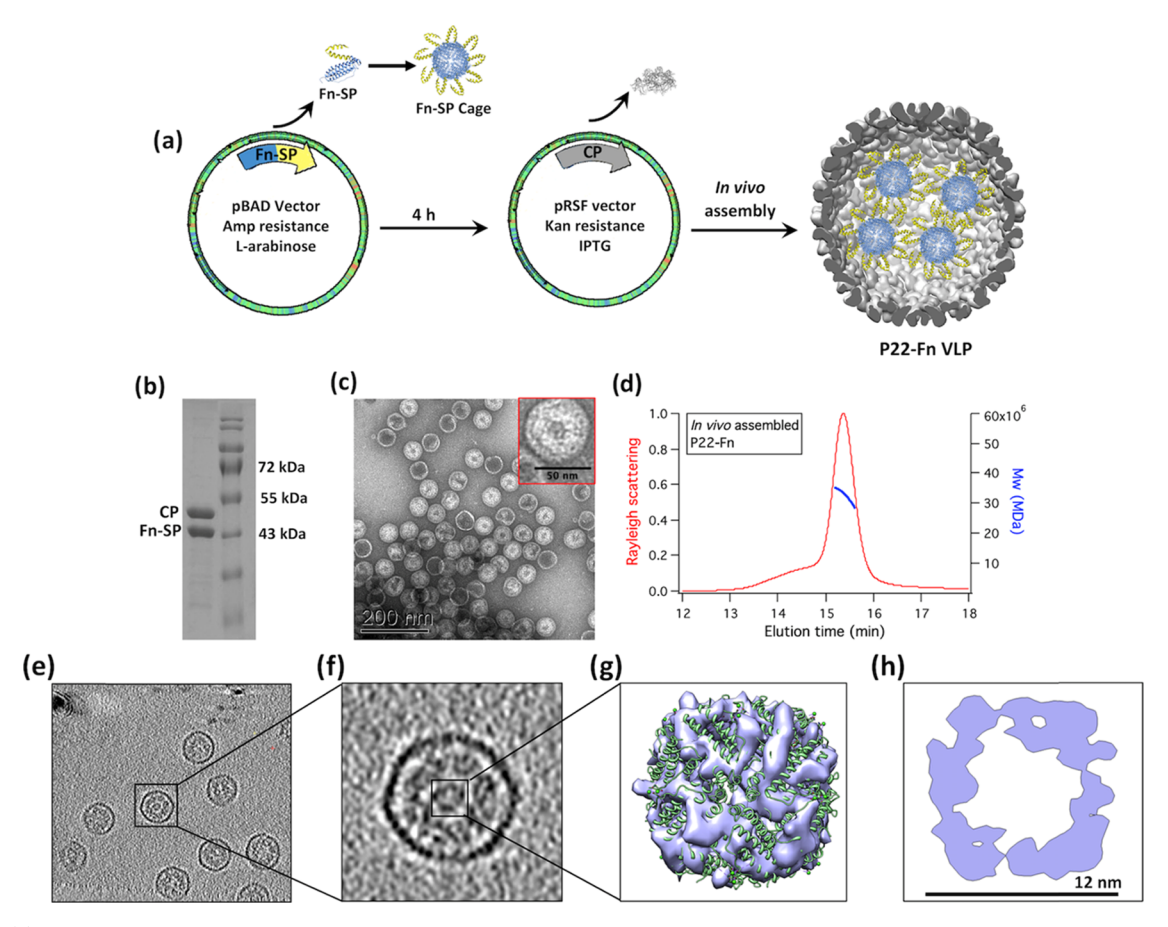


Figure 3. (a) Schematic showing the expression and assembly of P22-Fn VLPs using the two-vector staggered expression approach. Fn-SP was expressed first and given time to assemble (4 h) prior to induction of the CP and subsequent P22 VLP capsid assembly. (b) SDS-PAGE showed both P22 coat protein (47 kDa) and Fn-SP fusion protein (40 kDa) bands. (c) TEM micrograph of purified P22-Fn VLPs showed 56.6 ± 1.0 nm spherical protein cages with Fn-cage-like density inside (inset). (d) Molar mass of P22-Fn by SEC-MALS was 32.6 ± 0.1 MDa, which corresponds to encapsulation of 324 Fn-SP subunits (13.5 Fn-SP cages); $R_{\rm g}$ was 24 ± 0.1 nm. (e, f) Cryo-ET reconstruction of P22-Fn VLPs showing cage-like density inside P22 VLPs. (g, h) Three-dimensional (3D) rendering of cage-like density inside P22 could be fit into the crystal structure of ferritin (PDB: 2FHA). The \sim 12 nm cage-like electron density corresponds to the Fn-SP cages encapsulated within P22.

However, it was not clear from the TEM whether the encapsulated Fn-SP subunits had assembled into the ferritin cage because the small cage-like morphology of Fn was not clearly resolved inside P22-Fn VLPs (Figure 2b, inset image). This could be due to incomplete assembly of the Fn-SP cage structure prior to the templated assembly of P22, resulting in encapsulation of Fn-SP subunits or only partially assembled Fn-SP cages. To explore the possibility that Fn-SP was encapsulated as subunits and not as a fully formed cage, we heated P22-Fn procapsid particles to 70 °C to form the P22-Fn in its expanded morphology (EX).62 The quaternary structure of Fn is stable to > 70 °C⁴⁸ and the size of the assembled Fncage is too large to allow it to escape through the pores in the P22 EX structure. The structural transformation of the P22 VLP was confirmed by native agarose gel, which is sensitive to the increase in the particle size (Figure 2d). This morphological transformation results in disrupting noncovalent association between CP and SP, 62 and thus any Fn-SP subunits would be released from the CP 62 and free Fn-SP subunits and/ or partially assembled Fn-SP cages could possibly assemble into the complete cage structure within the EX P22. Purified P22-Fn EX showed the presence of both Fn-SP and CP bands in the SDS-PAGE gel (Figure 2a Lane-3), confirming retention of Fn-SP inside P22 after heating. TEM images of P22-Fn EX showed a slightly larger particle size (64.6 \pm 1.6 nm) than P22-

Fn PC due to P22 expansion (Figure 2e). TEM also revealed the apparent presence of small cage-like structures inside the P22 VLP (Figure 2e inset image), suggesting the presence of assembled Fn-SP cages. Molecular weight assessment of purified P22-Fn EX using SEC-MALS was observed to be 32.36 ± 0.21 MDa, which suggests that approximately 320 Fn-SP subunits (i.e., 13 Fn-SP cages if assembled) were retained (Figure 2f). This confirms that the assembled Fn-SP cages are retained within the capsid after the morphological transformation from PC to EX. From these data, we can infer that the simultaneous co-expression of Fn-SP and CP using the single-vector system may not provide optimal control over the self-assembly of the small (Fn) cage prior to the directed assembly and encapsulation by the larger P22 cage. However, disruption of the SP-CP interaction in the EX form appears to allow encapsulated Fn-SP subunits to assemble into the Fncage-like structure inside the P22.

Sequential Expression of Fn-SP and CP Using Two Vectors. To ensure assembly of Fn-SP into its cage-like architecture prior to encapsulation in the P22 VLP, the Fn-SP and CP were expressed sequentially (Figure 3a). A sequential expression system using temporal expression from two vectors has previously been demonstrated for directed protein cargo encapsulation in P22 where proper folding and/or maturation of a cargo protein was required prior to encapsulation. ^{58,72,73} E.

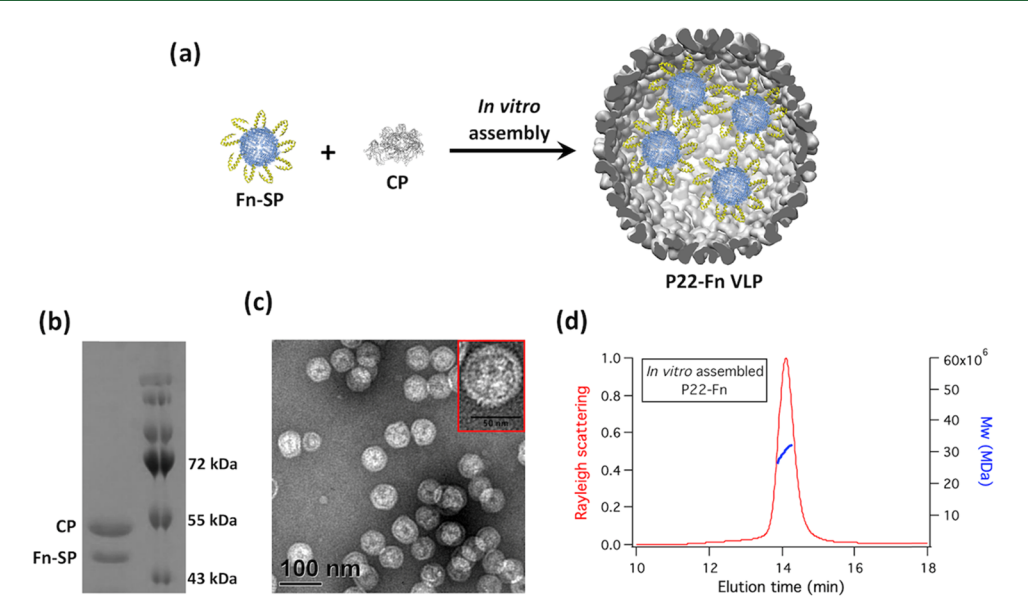


Figure 4. Characterization of purified P22-Fn VLP self-assembled *in vitro* from Fn-SP and CP in a 1.1:1 subunit molar ratio. (a) Schematic showing formation of P22-Fn VLPs using an *in vitro* self-assembly approach. (b) SDS-PAGE analysis of purified P22-Fn VLPs showed the presence of P22 coat protein (47 kDa) and Fn-SP fusion protein (40 kDa) bands confirming the encapsulation of Fn-SP. (c) TEM micrograph of purified P22-Fn VLPs (scale bar: 100 nm) showed 57.8 \pm 1.4 nm spherical protein cages similar in morphology to that of *in vivo* assembled P22-Fn. (d) SEC-MALS analysis of monodispersed P22-Fn VLPs revealed the molar mass of 30.3 \pm 0.1 MDa corresponding to encapsulation of 11.1 \pm 0.1 Fn-SP cages inside P22; R_{ν} was observed to be 23.5 \pm 0.06 nm.

coli with two vectors, encoding Fn-SP and CP, was first induced for Fn-SP production for 4 h, allowing sufficient time for Fn-SP subunits to self-assemble into the Fn-cage, followed by induction of CP expression for 3 h where the SP fused on the Fn-SP cage-templated CP assembly to form the P22-Fn VLP (Figure 3a). SDS-PAGE analysis on purified VLPs confirmed the presence of two protein bands, which are consistent with the molecular weights of Fn-SP and CP (Figure 3b) subunits. P22-Fn particles of 56.6 \pm 1.0 nm diameter, indistinguishable from wtP22 VLP, were observed by TEM (Figures 3c and S2). This sample more clearly showed the presence of small Fn-cage-like density inside the larger P22 VLP even without morphological transformation to the expanded form (Figure 3c, inset image), unlike the coexpression sample shown in Figure 2b. Mass spectrometry analysis of P22-Fn particles provided subunit molecular weights (M_w) of 39 998 Da and 46 625 Da, which agreed with calculated M_w of 39 996 Da for the Fn-SP subunit and 46 621 Da for the coat protein, respectively (Figure S3).

To confirm the formation of the P22-Fn nested structure and verify encapsulation of the smaller Fn-cage inside P22, single particle analysis, by cryo-electron tomography (cryo-ET), was undertaken. Unlike conventional electron microscopy, cryo-ET provided three-dimensional information of single P22-Fn VLP synthesized using the sequential expression approach. Cryo-ET reconstruction of P22-Fn VLPs clearly showed the presence of small cage-like densities inside the \sim 57 nm P22 VLP (Figure 3e,f). Subtomography volumes containing individual Fn cages were computationally selected from the cryo-ET reconstruction of P22-Fn VLPs and fit with the crystal structure of the human ferritin protein (Figure 3g,h) (PDB: 2FHA).⁴⁸ Good agreement of subtomography densities of 12 nm diameter small cage structures inside P22 with overall structure of the human ferritin protein confirmed the encapsulation of assembled Fn-SP cages inside P22 and the formation of the P22-Fn nested structure.

Molecular weight analysis by SEC-MALS of P22-Fn samples prepared using the sequential expression of Fn-SP and CP was observed to be 32.6 \pm 0.1 MDa. This corresponds to the encapsulation of 324 Fn-SP subunits (13 Fn-SP cages) per P22 VLP (Figure 3d), which is similar to the simultaneous coexpression approach (Figure 2c). By considering the volume of the P22 VLP interior cavity 74 (46 452 nm³) and Fn-SP (1440 nm³), we estimate a packing density for Fn-SP within P22 of approximately 40%. This is similar to previously reported cargo packaging densities within P22 51,74,75 and may represent a required number of scaffold proteins 63 or a requirement for the volume occupancy of the cargo to complete the capsid self-assembly. 76

Stability of the P22-Fn Nested Structure. P22 procapsid VLPs (~56 nm), when heated at 75 °C for 20 min, change their morphology to form a wiffle ball structure (~64 nm) loosing twelve pentamers from the icosahedral vertices and forming ~10 nm large pores. 62,64 The stability of the nested P22 VLPs was tested for maintenance of the cage architecture along with retention of Fn cargo inside after heating P22-Fn PC VLPs to 75 °C. The change in the morphology of P22-Fn VLPs was assessed by the differences in PC and WB VLP mobility on native agarose gel (Figure S4a) and the change in retention time, from 14.8 min (PC) to 14.5 min (WB), on SEC-MALS (Figure S5a,d). SEC-MALS also provided $M_{\rm w}$ of 32.1 \pm 0.2 MDa (PC) and 30.3 \pm 0.3 MDa (WB) corresponding to the presence of 13.0 \pm 0.2 Fn cages before heating and 13.9 \pm 0.3 Fn cages after heating P22-Fn VLPs, and reduction in M_w (by 1.8 MDa) is due to the loss of 60 CP subunits from twelve pentamers at icosahedral vertices upon change in the VLP morphology. SDS-PAGE analysis on purified VLPs after heating showed the Fn-SP subunit band and confirmed retention of Fn-SP cages inside P22 VLPs (Figure S4b). Characterization of these particles by TEM (Figure S5b,e) confirmed the change in the VLP morphology from the PC (57.2 \pm 1.4 nm) to WB (63.1 \pm 0.9 nm) structure

with Fn-cage-like density inside. Hydrodynamic diameter obtained from DLS (Figure S5c,f) was observed to be 57.7 \pm 0.7 nm (PC) and 63.9 \pm 0.9 nm (WB) and was consistent with the TEM results confirming that P22-Fn nested VLPs are stable.

In Vitro Assembly of the P22 VLP-Encapsulating Fn-**SP Cage.** *In vitro* assembly of CP subunits and cargo-SP fusion proteins has been demonstrated as an alternative approach to prepare P22 VLP with encapsulated cargo. 58,77 The in vitro assembly approach allows tuning of the ratio of cargo-SP and CP, which leads to control over cargo loading density inside the P22 VLP. 58 Here, we mixed Fn-SP and CP (Figure 4a) at subunit molar ratios of 0.55:1, 1.1:1, and 1.6:1 to investigate the control over Fn-SP loading within P22 VLP. As described in the Experimental Section, the purified Fn-SP cage was added to the CP subunit in the presence of 1.5 M GuHCl. The Fn-SP cage was confirmed to maintain its cage-like quaternary structure in 1.5 M GuHCl (Figure S6), but the CP remained mostly unfolded.⁶⁵ The removal of the GuHCl by dialysis resulted in refolding of CP and subsequent assembly into P22 VLP together with Fn-SP encapsulation. Analysis of these particles by TEM and SDS-PAGE confirmed the assembly of 57.8 ± 1.4 nm diameter P22 VLPs composed of Fn-SP and CP (Figure 4). From the TEM, the presence of small cage-like Fn particles inside the P22 VLP was observed (Figures 4c and S7a,c), similar to P22-Fn VLP developed via in vivo assembly with sequential protein expression (Figure 3c). Analysis of the in vitro assembled particles by SEC-MALS (Figure 4d) revealed a radius of gyration ($R_g = 23.5 \pm 0.06$ nm) similar

to P22-Fn assembled in vivo ($R_{\rm g}=24\pm0.1~{\rm nm}$) (Figure 3d). From the $M_{\rm w}$ measurements by MALS, the number of the Fn-SP cage encapsulated inside VLP was calculated to be very similar regardless of the input Fn-SP to CP ratio. VLPs prepared at the three different ratios exhibited molecular weights of 29.6 \pm 0.1, 30.3 \pm 0.1m, and 30.6 \pm 0.1 MDa corresponding to encapsulation of 250 Fn-SP subunits (10.4 \pm 0.1 cages), 265 subunits (11.1 \pm 0.1 cages), and 270 subunits (11.4 \pm 0.1 Fn-SP cages), respectively (Figures 4d and S7b,d). Furthermore, the Fn-SP packing efficiency is quite similar to that observed in P22-Fn produced by in vivo assembly approaches. These results suggest that there could be an optimal number of scaffold proteins or optimal volume of interior cargo occupancy necessary to direct assembly conditions tested.

Thrombin Digestion and in Vitro Iron Mineralization in Fn and P22 VLP Variants. The iron oxide mineralization capability of the Fn-SP cage (not encapsulated in P22) was assessed and compared with the wild-type human ferritin cage (Fn) as a control. To test the role of SP fusion to ferritin in the iron oxide mineralization, we took advantage of a thrombin protease site engineered in the Fn-SP fusion protein between Fn and SP (see SI, Section 2 for sequence details) to cleave the SP from the Fn-SP cage. Purified Fn-SP cages, when treated with thrombin, resulted in the formation of Fn-linker cages (22 kDa, Subunit M_w) and linker-SP (18.1 kDa) proteins as cleavage products, which were confirmed by SDS-PAGE analysis (Figure S8a). Fn-linker cages were purified by sizeexclusion chromatography (Figure S8b). TEM characterization showed 14.4 \pm 0.6 nm Fn-SP cages and 12.6 \pm 1.1 nm Fnlinker cages before and after thrombin digestion, respectively, where Fn-linker cages looked morphologically similar to wtFn cages (Figures S8c,e and 1d). DLS analysis further confirmed

the cleavage of 15.5 \pm 0.4 nm Fn-SP cages into 12.8 \pm 0.2 nm Fn-linker cages upon thrombin treatment (Figure S8d,f). Under similar experimental conditions, thrombin digestion was also carried out on P22-Fn WB VLPs. P22-Fn WB (thrombin) showed similar mobility on a native agarose gel, suggesting maintenance of the P22 cage structure similar to P22-Fn WB VLPs (Figure S9a). The cleavage of Fn-SP inside P22 was confirmed by SDS-PAGE analysis (Figure S9b). TEM images of purified P22-Fn WB (thrombin) showed 63.2 ± 0.7 nm VLPs with Fn-cage-like density inside confirming retention of Fn-linker cages within P22 after the thrombin treatment (Figure S9c). Particle sizes obtained from DLS analysis were in agreement with the TEM results showing 63.9 ± 0.2 nm VLPs (Figure S9d). SEC-MALS characterization of purified P22-Fn (thrombin) VLPs provided $M_{\rm w}$ of 27.6 \pm 0.6 MDa (Figure S9e), which is a 2.8 \pm 0.2 MDa lower M_w than before thrombin digestion (Figure S5d), consistent with the loss of linker-SP after the cleavage from Fn-SP cages inside P22.

We tested the iron oxide mineralization capability of Fn-cage variants (Fn-SP, Fn-linker, Fn control) under total loading of 2000 Fe²⁺ per cage and P22 VLP variants P22-Fn WB and P22-Fn WB (thrombin) under total loading of 21 600 Fe²⁺ per VLP. The proteins were incubated with aliquots of Fe(II) (as ammonium iron(II) sulfate) and allowed to air oxidize to form iron oxide (Fe₂O₃), and the mineralization reaction was monitored at 420 nm (iron oxide mineral) and 800 nm (scattering due to bulk precipitate) and compared to a protein-free control reaction.

Protein-free control reaction and Fn-SP showed an increase in scattering at 800 nm (Figure S10a,b) consistent with mineralization in the bulk medium and not confined to the interior of the Fn-cage, which was further confirmed by physical observation of a red-brown precipitate. In contrast, Fn control and Fn-linker cages showed an increase in the absorbance at 420 nm during the course of the mineralization reaction with little to no increase at 800 nm, suggesting formation of iron oxide mineral inside the Fn-cage without formation of bulk aggregates (Figure S10c,d). While the Cterminus of Fn generally does not seem to play an important role in the iron oxidation,⁷⁸ it is clear that the fusion of the SP₁₄₁ to the C-terminus of ferritin disrupts the mineralization activity, although it does not prevent the 24-subunit cage assembly. Mineralization of the Fn-SP and Fn-linker cages encapsulated inside P22 showed an increase in the absorbance at 420 nm with a slight increase in scattering at 800 nm during the course of the mineralization reaction in both P22 VLP variants (Figure S10e,f).

To confirm that increase in the absorbance at 420 nm was indeed due to mineral formation and not due to contribution from large aggregates, TEM analysis was performed to observe mineral particles (Figure S11) and protein cages were imaged by negative staining with uranyl acetate. The no-protein control showed larger sized bulk precipitate formation of 20.2 \pm 19.3 μ m, whereas Fn control showed formation of constrained mineral with the core diameter of 4.7 ± 1 nm. The Fn-SP cage failed to mineralize iron oxide in its interior cavity (Figure S11) and showed particles with diameter of 20.1 ± 9 nm, whereas Fn-linker showed constrained iron oxide mineral with core diameter of 6.1 ± 1.3 nm. This is consistent with our assertion that SP fusion to Fn hindered Fe²⁺ entry into Fn and cleavage of the SP allowed Fn-linker cages to mineralize iron oxide similar to Fn (Figure S11). Furthermore, P22-Fn WB and P22-Fn WB (thrombin) both showed mineral

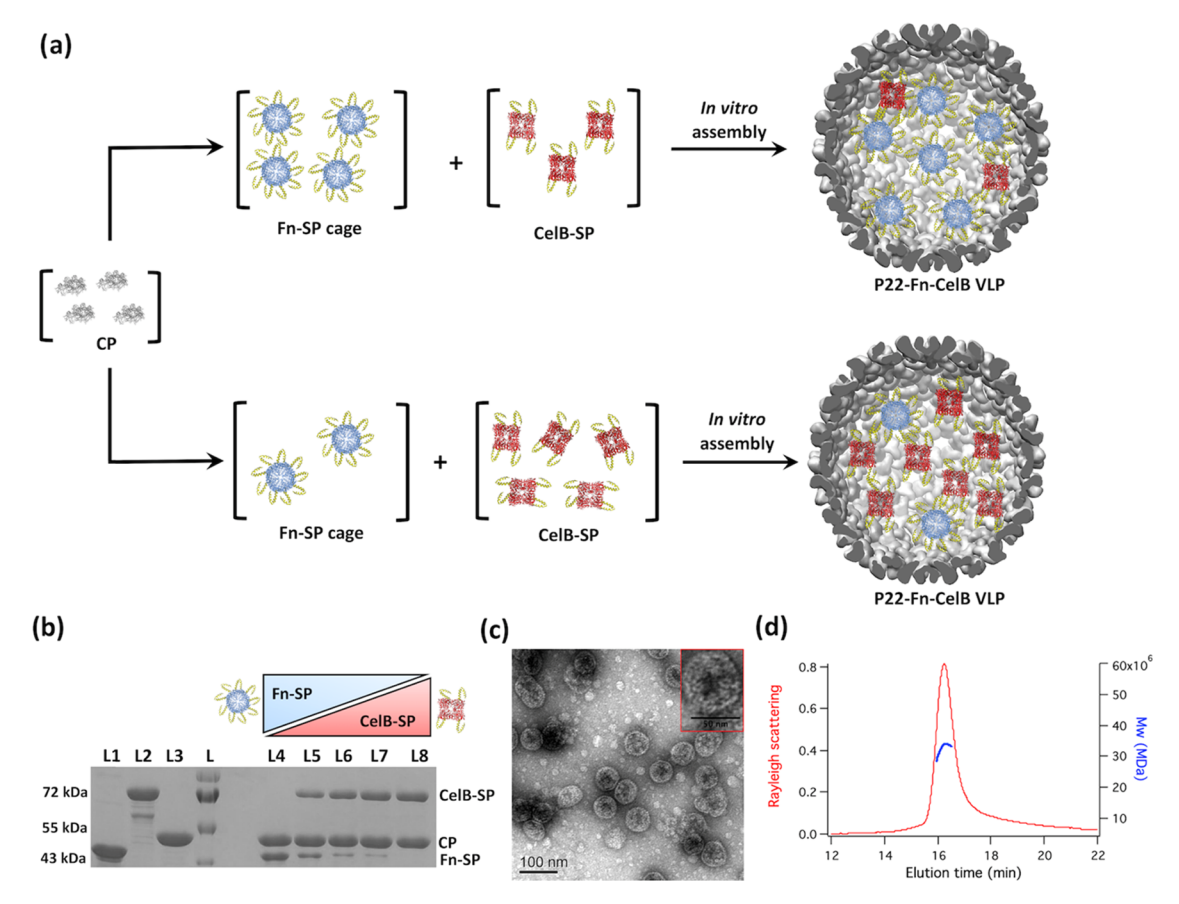


Figure 5. Characterization of co-assembled Fn-SP cages and CelB-SP inside P22 VLPs. (a) Schematic representation of the co-assembly of Fn-SP and CelB-SP to form P22-Fn-CelB VLPs using the *in vitro* self-assembly approach. Purified Fn-SP cages and CelB-SP tetramers were mixed in varying stoichiometric ratios to control cargo loading density. (b) SDS-PAGE analysis showing the purity of Fn-SP and CelB-SP cargo along with the coat protein used in this work (Lane L1, L2, and L3). Lane L is the standard protein ladder. Lane 4 and Lane 8 represent P22 VLPs assembled only with Fn-SP cages or CelB-SP cargo. Lane 5, 6, and 7 represent P22-Fn-CelB co-assembled VLPs with input subunit ratios of Fn-SP/CelB-SP during assembly corresponding to 1:1, 1;3, and 1:6. At 1:1, 1:3, and 1:6 input subunit ratios of Fn-SP/CelB-SP, the output subunit ratios were observed to be 1:0.7, 1:1.9, and 1:3.9, respectively, after densitometry analysis on the SDS-PAGE gel. (c) Transmission electron microscopy (TEM) image of P22 VLPs where the 1:1 subunit molar ratio of Fn-SP/CelB-SP was used for assembly showing a morphology and size similar to P22 VLPs. The TEM inset image showing the Fn-cage-like density inside 58.9 ± 1.7 nm P22 VLPs suggesting Fn-SP encapsulated as cages inside co-assembled P22 similar to P22-Fn. (d) Molar mass from SEC-MALS was observed to be 32.82 ± 0.01 MDa, whereas R_g and R_h of VLPs were observed to be 22.1 ± 0.1 nm, and 27.2 ± 0.43 nm, respectively.

particles of 64.5 ± 5.8 and 64.3 ± 3.6 nm, respectively (Figure S11), suggesting the formation of iron oxide mineral within P22 VLP interior cavity and around P22 VLP exterior. This observation is similar to our previous reports in the literature where P22 VLPs with SP₁₄₁ inside were able to direct iron oxide mineralization within VLP. The interior and exterior surfaces of P22 are both significantly negatively charged, which is possibly sufficient to initiate nonspecific Fe₂O₃ mineralization at those interfaces.

In Vitro Assembly of the P22 VLP-Encapsulating Fn-SP Cage and CelB-SP Tetramer. To create a hierarchical compartment with multiple protein cargos as a cell-like mimic, we used an *in vitro* co-assembly approach to co-encapsulate preformed Fn-SP cages as subcompartments and the glucosidase enzyme CelB-SP as accompanying co-packaged macromolecules (Figure 5a). The *in vitro* co-assembly of CP subunits with cargo-SP and wtSP has been previously demonstrated as a powerful method to encapsulate multiple types of cargo with controlled loading stoichiometry inside P22 VLPs. Sp. Here, we used this approach to co-encapsulate Fn and CelB cargo. Different subunit molar ratios of Fn-SP/CelB-SP (1:1, 1:3, and 1:6) were added to CP subunits in the

presence of 1.5 M GuHCl. Dialyzing out GuHCl from the assembly mixtures resulted in formation of P22-Fn-CelB VLPs where both Fn-SP cages and CelB-SP were co-encapsulated as cargo inside the P22. SDS-PAGE confirmed the presence of Fn-SP, CelB-SP, and P22 CP in the purified material under all co-assembly conditions tested (Figure 5b Lanes 5, 6, and 7), indicating successful co-encapsulation of both Fn-SP and CelB-SP cargo inside P22. Densitometry analysis of the SDS-PAGE gels revealed that the relative amount of each cargo encapsulated was proportional to the input stoichiometry used during co-assembly (Figure S15). These results demonstrate direct control over the average loading stoichiometry of two different macromolecular cargo species inside the P22, which depends on the input cargo stoichiometric ratios.

TEM of P22 VLPs co-assembled with both Fn-SP and CelB-SP at a 1:1 subunit molar ratio showed the formation of spherical P22 particles with average diameter of 59 ± 1.7 nm, morphologically similar to native P22 VLPs (Figures 5c and S2). A TEM image of a single particle showed the presence of a small Fn-cage-like density inside the P22 VLPs (Figure 5c, inset image), an observation similar to P22-Fn VLPs (Figure

4c). Similar Fn-cage-like density was also observed inside coassembled P22 particles where assembly was carried out at 1:3 and 1:6 subunit molar ratios of Fn-SP/CelB-SP (Figure S16).

SEC-MALS provided average molar mass, R_g and R_h , of P22-Fn-CelB co-assembled particles (Figures 5d, S16 and Table S1). The molar mass of the empty shell was subtracted from the mass of the co-assembled particle to get the total molar mass contribution of Fn-SP and CelB-SP. The ratio of Fn-SP to CelB-SP in the three co-assembly reactions obtained from densitometry analysis of SDS-PAGE Gel (Figure 5b) was used together with the average cargo molar mass obtained from SEC-MALS to estimate the average number of Fn-SP cages and CelB-SP tetramers per P22 capsid (See the Experimental Section and Supporting Information, Section 12 for details). Roughly, 143 ± 0.2 Fn-SP subunits (5.9 ± 0.01 cages) and 100 \pm 0.04 CelB-SP subunits (25.1 \pm 0.01 tetramers) were encapsulated when the input subunit ratio of 1:1 was used during co-assembly. For 1:3 and 1:6 input subunit ratios, 68 \pm 2 and 37 \pm 0.5 Fn-SP subunits along with 129 \pm 3 and 143 \pm 1 CelB-SP subunits were co-encapsulated, respectively (Table S2). These results show broad control over the degree of compartmentalization and cargo packing stoichiometry inside a complex hierarchical structure at the nanoscale. From the volume of Fn-SP (~1440 nm3) and the CelB-SP tetramer $(\sim 660 \text{ nm}^3)$, ⁷⁴ we estimate the total macromolecular packing density for P22-Fn-CelB to be in the range of 54-56% for the co-encapsulation reactions (Table S2). Based on the number of Fn-SP subunits and CelB-SP subunits co-encapsulated inside P22, we calculated the total internal cargo concentrations, which is reported here as the molarity of confinement (M_{conf}) . The M_{conf} for the co-encapsulated P22-Fn-CelB ranges from 6.4 to 8.7 mM (Table S2), which is similar to the expected macromolecular concentration within a cell. 59,82

P22-Fn-CelB Glucosidase Enzyme Activity. To assess whether the CelB glucosidase enzyme, co-encapsulated with Fn, retains catalytic activity, we determined the kinetic parameters using 4-nitrophenyl- β -glucopyranoside (PNPG) as a substrate, which upon cleavage of the glycosidic bond releases 4-nitrophenol that was monitored spectrophotometrically at 405 nm.⁵¹ P22-CelB was used as a control and is reported to exhibit the same kinetic parameters as the free CelB enzyme, suggesting that the enzyme CelB is insensitive to crowding and confinement effects. 51 The P22-CelB and P22-Fn-CelB (Fn-SP/CelB-SP 1:3) showed similar catalytic activity when tested under the same enzyme concentrations (Figure S17 and Table S3), confirming that the co-encapsulated CelB enzyme is catalytically as active as previously determined for free and encapsulated CelB. A systematic comparison of the kinetic behavior of the enzyme at different loading ratios (Fn-SP/CelB-SP 1:1 and 1:6) revealed only small differences in the catalytic activity (Figure S17 and Table S3) that are hard to interpret as being solely due to crowding effects.

■ CONLCUSIONS

Hierarchically organized compartments in organisms, such as cells or subcellular compartments, control and sequester important biochemical reactions. Here, we have presented a proof-of-concept study using the P22 VLP capsid to mimic in our synthetic design some aspects of an eukaryotic cell, notably the formation of subcompartment isolation within a larger compartment. We have demonstrated that we can encapsulate multiple macromolecular cargos, one which is itself a protein cage with its own interior environment and thus acting as a

subcompartment and the other an active enzyme macromolecule. We have demonstrated the formation of a complex protein-based hierarchical structure, which exhibits some of the features of a minimal synthetic cell using multiple protein selfassembly processes by design. Both in vivo and in vitro selfassembly approaches were explored to form nested compartment structures. Our results demonstrate encapsulation of 10-13 copies of the 960 kDa Fn-SP cages with 14 nm diameter as the smaller compartment inside the 58 nm P22 VLP. Using controlled in vitro assembly, we also demonstrated copackaging of the active CelB enzyme, together with the ferritin subcompartment, thus creating a densely packed macromolecular environment inside the sequestered volume of the P22 capsid. The ratio of the encapsulated Fn to CelB cargo could be tuned through changes in the self-assembly input stoichiometry to vary the degree of compartmentalization. To our knowledge, it is the first time when control over degree of compartmentalization has been demonstrated in protein-based systems with the modulating stoichiometry of multiple cargo loading. Our findings show that multiple different protein cargos can be encapsulated inside P22 VLPs in highly crowded and cell-like macromolecular concentrations while retaining some of their catalytic efficiency. The successful design and assembly of hierarchically complex materials opens up future opportunities to develop organelle-mimic synthetic materials with desired biochemical functions.

ASSOCIATED CONTENT

Supporting Information

The Supporting Information is available free of charge at https://pubs.acs.org/doi/10.1021/acs.biomac.0c00030.

DNA and amino acid sequences of proteins, purification and characterization of Fn-SP, CelB-SP, P22-Fn, and P22-Fn-CelB co-assembled VLPs, stability of nested P22-Fn VLPs, calculation for determining the number of cargo encapsulated, iron oxide mineralization of Fn and P22 variants, and the catalytic activity of the enzyme CelB co-encapsulated with Fn-SP in P22 VLPs (PDF)

AUTHOR INFORMATION

Corresponding Author

Trevor Douglas — Department of Chemistry, Indiana University, Bloomington, Indiana 47405, United States; orcid.org/0000-0002-7882-2704; Phone: (812) 856-6936; Email: trevdoug@indiana.edu

Authors

Hitesh Kumar Waghwani — Department of Chemistry, Indiana University, Bloomington, Indiana 47405, United States

Masaki Uchida — Department of Chemistry, Indiana University, Bloomington, Indiana 47405, United States; Department of Chemistry, California State University Fresno, Fresno, California 93740, United States; Orcid.org/0000-0003-0710-8834

Chi-Yu Fu — Department of Molecular Biology, The Scripps Research Institute, La Jolla, California 92037, United States; Institute of Cellular and Organismic Biology, Academia Sinica, Taipei 115, Taiwan

Benjamin LaFrance — Department of Chemistry and Biochemistry, Montana State University, Bozeman, Montana 59717, United States; oorcid.org/0000-0003-0229-5255

Jhanvi Sharma – Department of Chemistry, Indiana University, Bloomington, Indiana 47405, United States; ocid.org/ 0000-0003-1985-560X

Kimberly McCoy — Department of Chemistry, Indiana University, Bloomington, Indiana 47405, United States

Complete contact information is available at: https://pubs.acs.org/10.1021/acs.biomac.0c00030

Notes

The authors declare no competing financial interest.

ACKNOWLEDGMENTS

T.D. and M.U. were supported by a grant from the U.S. Department of Energy, Office of Basic Energy Sciences, Division of Materials Sciences and Engineering (DE-SC0016155). H.K.W. was supported by a grant from the National Science Foundation (NSF-BMAT DMR-1507282) and M.U. was additionally supported by a National Science Foundation grant (NSF-NM CMMI-1922883). We thank Prof. John E Johnson for access to electron microscopy instrument, the IU Electron Microscopy Center, the IU Nanoscale Characterization Facility, the IU Mass Spectrometry Facility, and the IU Laboratory for Biological Mass Spectrometry for access to their instrumentation.

REFERENCES

- (1) Cai, F.; Sutter, M.; Bernstein, S. L.; Kinney, J. N.; Kerfeld, C. A. Engineering bacterial microcompartment shells: chimeric shell proteins and chimeric carboxysome shells. *ACS Synth. Biol.* **2015**, *4*, 444–453.
- (2) Dzieciol, A. J.; Mann, S. Designs for life: protocell models in the laboratory. *Chem. Soc. Rev.* **2012**, *41*, 79–85.
- (3) Li, M.; Huang, X.; Tang, T. Y.; Mann, S. Synthetic cellularity based on non-lipid micro-compartments and protocell models. *Curr. Opin. Chem. Biol.* **2014**, 22, 1–11.
- (4) Martin, W.; Koonin, E. V. A positive definition of prokaryotes. *Nature* **2006**, 442, 868.
- (5) Kerfeld, C. A.; Erbilgin, O. Bacterial microcompartments and the modular construction of microbial metabolism. *Trends Microbiol.* **2015**, 23, 22–34.
- (6) Kostiainen, M. A.; Kasyutich, O.; Cornelissen, J. J. L. M.; Nolte, R. J. M. Self-assembly and optically triggered disassembly of hierarchical dendron-virus complexes. *Nat. Chem.* **2010**, *2*, 394–399.
- (7) Sontz, P. A.; Bailey, J. B.; Aln, S.; Tezcan, F. A. A Metal Organic Framework with Spherical Protein Nodes: Rational Chemical Design of 3D Protein Crystals. *J. Am. Chem. Soc.* **2015**, *137*, 11598–11601.
- (8) Künzle, M.; Eckert, T.; Beck, T. Binary Protein Crystals for the Assembly of Inorganic Nanoparticle Superlattices. *J. Am. Chem. Soc.* **2016**, *138*, 12731–12734.
- (9) Uchida, M.; LaFrance, B.; Broomell, C. C.; Prevelige, P. E.; Douglas, T. Higher Order Assembly of Virus-like Particles (VLPs) Mediated by Multi-valent Protein Linkers. *Small* **2015**, *11*, 1562–1570
- (10) Uchida, M.; McCoy, K.; Fukuto, M.; Yang, L.; Yoshimura, H.; Miettinen, H. M.; LaFrance, B.; Patterson, D. P.; Schwarz, B.; Karty, J. A.; Prevelige, P. E., Jr; Lee, B.; Douglas, T. Modular Self-Assembly of Protein Cage Lattices for Multistep Catalysis. *ACS Nano* **2018**, *12*, 942–953.
- (11) Patterson, D. P.; Schwarz, B.; Waters, R. S.; Gedeon, T.; Douglas, T. Encapsulation of an enzyme cascade within the bacteriophage P22 virus-like particle. *ACS Chem. Biol.* **2014**, *9*, 359–365.
- (12) Frey, R.; Mantri, S.; Rocca, M.; Hilvert, D. Bottom-up Construction of a Primordial Carboxysome Mimic. *J. Am. Chem. Soc.* **2016**, *138*, 10072–10075.

- (13) Brasch, M.; Putri, R. M.; de Ruiter, M. V.; Luque, D.; Koay, M. S.; Caston, J. R.; Cornelissen, J. J. Assembling Enzymatic Cascade Pathways inside Virus-Based Nanocages Using Dual-Tasking Nucleic Acid Tags. J. Am. Chem. Soc. 2017, 139, 1512—1519.
- (14) Lau, Y. H.; Giessen, T. W.; Altenburg, W. J.; Silver, P. A. Prokaryotic nanocompartments form synthetic organelles in a eukaryote. *Nat. Commun.* **2018**, *9*, No. 1311.
- (15) Beck, T.; Tetter, S.; Künzle, M.; Hilvert, D. Construction of Matryoshka-Type Structures from Supercharged Protein Nanocages. *Angew. Chem., Int. Ed.* **2015**, *54*, 937–940.
- (16) Martino, C.; deMello, A. J. Droplet-based microfluidics for artificial cell generation: a brief review. *Interface Focus* **2016**, *6*, 20160011.
- (17) Elani, Y. Construction of membrane-bound artificial cells using microfluidics: a new frontier in bottom-up synthetic biology. *Biochem. Soc. Trans* **2016**, *44*, 723–730.
- (18) Elani, Y.; Solvas, X. C. I.; Edel, J. B.; Law, R. V.; Ces, O. Microfluidic generation of encapsulated droplet interface bilayer networks (multisomes) and their use as cell-like reactors. *Chem. Commun.* **2016**, *52*, 5961–5964.
- (19) Salehi-Reyhani, A.; Ces, O.; Elani, Y. Artificial cell mimics as simplified models for the study of cell biology. *Exp. Biol. Med.* **2017**, 242, 1309–1317.
- (20) Matosevic, S.; Paegel, B. M. Stepwise Synthesis of Giant Unilamellar Vesicles on a Microfluidic Assembly Line. *J. Am. Chem. Soc.* **2011**, *133*, 2798–2800.
- (21) Matosevic, S.; Paegel, B. M. Layer-by-layer cell membrane assembly. *Nat. Chem.* **2013**, *5*, 958–963.
- (22) Li, M.; Green, D. C.; Anderson, J. L. R.; Binks, B. P.; Mann, S. In vitro gene expression and enzyme catalysis in bio-inorganic protocells. *Chem. Sci.* **2011**, *2*, 1739–1745.
- (23) Huang, X.; Li, M.; Green, D. C.; Williams, D. S.; Patil, A. J.; Mann, S. Interfacial assembly of protein-polymer nano-conjugates into stimulus-responsive biomimetic protocells. *Nat. Commun.* **2013**, *4*, No. 2239.
- (24) Tang, T.-Y. D.; Hak, C. R. C.; Thompson, A. J.; Kuimova, M. K.; Williams, D. S.; Perriman, A. W.; Mann, S. Fatty acid membrane assembly on coacervate microdroplets as a step towards a hybrid protocell model. *Nat. Chem.* **2014**, *6*, 527–533.
- (25) Marguet, M.; Sandre, O.; Lecommandoux, S. Polymersomes in "gelly" polymersomes: toward structural cell mimicry. *Langmuir* **2012**, 28, 2035–2043.
- (26) Marguet, M.; Edembe, L.; Lecommandoux, S. Polymersomes in polymersomes: multiple loading and permeability control. *Angew. Chem., Int. Ed.* **2012**, *51*, 1173–1176.
- (27) Discher, D. E.; Eisenberg, A. Polymer vesicles. *Science* **2002**, 297, 967–973.
- (28) Mason, A. F.; Yewdall, N. A.; Welzen, P. L. W.; Shao, J. X.; van Stevendaal, M.; van Hest, J. C. M.; Williams, D. S.; Abdelmohsen, L. K. E. A. Mimicking Cellular Compartmentalization in a Hierarchical Protocell through Spontaneous Spatial Organization. *ACS Cent. Sci.* **2019**, *5*, 1360–1365.
- (29) Walker, S. A.; Kennedy, M. T.; Zasadzinski, J. A. Encapsulation of bilayer vesicles by self-assembly. *Nature* **1997**, 387, 61–64.
- (30) Kisak, E. T.; Coldren, B.; Evans, C. A.; Boyer, C.; Zasadzinski, J. A. The vesosome A multicompartment drug delivery vehicle. *Curr. Med. Chem.* **2004**, *11*, 199–219.
- (31) Boyer, C.; Zasadzinski, J. A. Multiple lipid compartments slow vesicle contents release in lipases and serum. ACS Nano 2007, 1, 176–182.
- (32) Berkland, C.; Kim, K. K.; Pack, D. W. Fabrication of PLG microspheres with precisely controlled and monodisperse size distributions. *J. Controlled Release* **2001**, *73*, 59–74.
- (33) Berkland, C.; Pollauf, E.; Pack, D. W.; Kim, K. Uniform double-walled polymer microspheres of controllable shell thickness. *J. Controlled Release* **2004**, *96*, 101–111.
- (34) Tran, V. T.; Benoit, J. P.; Venier-Julienne, M. C. Why and how to prepare biodegradable, monodispersed, polymeric microparticles in the field of pharmacy? *Int. J. Pharm.* **2011**, 407, 1–11.

- (35) Göpfrich, K.; Haller, B.; Staufer, O.; Dreher, Y.; Mersdorf, U.; Platzman, I.; Spatz, J. P. One-Pot Assembly of Complex Giant Unilamellar Vesicle-Based Synthetic Cells. *ACS Synth. Biol.* **2019**, *8*, 937–947.
- (36) Lee, K. Y.; Park, S. J.; Lee, K. A.; Kim, S. H.; Kim, H.; Meroz, Y.; Mahadevan, L.; Jung, K. H.; Ahn, T. K.; Parker, K. K.; Shin, K. Photosynthetic artificial organelles sustain and control ATP-dependent reactions in a protocellular system. *Nat. Biotechnol.* **2018**, *36*, 530–535.
- (37) Fu, Z.; Ochsner, M. A.; de Hoog, H. P. M.; Tomczak, N.; Nallani, M. Multicompartmentalized polymersomes for selective encapsulation of biomacromolecules. *Chem. Commun.* **2011**, 47, 2862–2864.
- (38) Kreft, O.; Skirtach, A. G.; Sukhorukov, G. B.; Mohwald, H. Remote control of bioreactions in multicompartment capsules. *Adv. Mater.* **2007**, *19*, 3142–3145.
- (39) Kreft, O.; Prevot, M.; Mohwald, H.; Sukhorukov, G. B. Shell-inshell microcapsules: A novel tool for integrated, spatially confined enzymatic reactions. *Angew. Chem., Int. Ed.* **2007**, *46*, 5605–5608.
- (40) Vladisavljević, G. T.; Kobayashi, I.; Nakajima, M. Production of uniform droplets using membrane, microchannel and microfluidic emulsification devices. *Microfluid. Nanofluid.* **2012**, *13*, 151–178.
- (41) Nakashima, T.; Shimizu, M.; Kukizaki, M. Particle control of emulsion by membrane emulsification and its applications. *Adv. Drug Delivery Rev.* **2000**, *45*, 47–56.
- (42) Chandrawati, R.; van Koeverden, M. P.; Lomas, H.; Caruso, F. Multicompartment Particle Assemblies for Bioinspired Encapsulated Reactions. *J. Phys. Chem. Lett.* **2011**, *2*, 2639–2649.
- (43) Sun, S. Y.; La Scola, B.; Bowman, V. D.; Ryan, C. M.; Whitelegge, J. P.; Raoult, D.; Rossmann, M. G. Structural Studies of the Sputnik Virophage. *J. Virol.* **2010**, *84*, 894–897.
- (44) Xiao, C.; Kuznetsov, Y. G.; Sun, S. Y.; Hafenstein, S. L.; Kostyuchenko, V. A.; Chipman, P. R.; Suzan-Monti, M.; Raoult, D.; McPherson, A.; Rossmann, M. G. Structural Studies of the Giant Mimivirus. *PLoS Biol.* **2009**, *7*, No. e1000092.
- (45) Sutter, M.; Boehringer, D.; Gutmann, S.; Guenther, S.; Prangishvili, D.; Loessner, M. J.; Stetter, K. O.; Weber-Ban, E.; Ban, N. Structural basis of enzyme encapsulation into a bacterial nanocompartment. *Nat. Struct. Mol. Biol.* **2008**, *15*, 939–947.
- (46) Rahmanpour, R.; Bugg, T. D. H. Assembly in vitro of Rhodococcus jostii RHA1 encapsulin and peroxidase DypB to form a nanocompartment. *FEBS J.* **2013**, *280*, 2097–2104.
- (47) McHugh, C. A.; Fontana, J.; Nemecek, D.; Cheng, N. Q.; Aksyuk, A. A.; Heymann, J. B.; Winkler, D. C.; Lam, A. S.; Wall, J. S.; Steven, A. C.; Hoiczyk, E. A virus capsid-like nanocompartment that stores iron and protects bacteria from oxidative stress. *EMBO J.* **2014**, 33, 1896—1911.
- (48) Hempstead, P. D.; Yewdall, S. J.; Fernie, A. R.; Lawson, D. M.; Artymiuk, P. J.; Rice, D. W.; Ford, G. C.; Harrison, P. M. Comparison of the three-dimensional structures of recombinant human H and horse L ferritins at high resolution. *J. Mol. Biol.* **1997**, 268, 424–448.
- (49) Uchida, M.; Kang, S.; Reichhardt, C.; Harlen, K.; Douglas, T. The ferritin superfamily: Supramolecular templates for materials synthesis. *Biochim. Biophys. Acta, Gen. Subj.* **2010**, *1800*, 834–845.
- (50) Tetter, S.; Hilvert, D. Enzyme Encapsulation by a Ferritin Cage. *Angew. Chem., Int. Ed.* **2017**, *56*, 14933–14936.
- (51) Patterson, D. P.; Schwarz, B.; El-Boubbou, K.; van der Oost, J.; Prevelige, P. E.; Douglas, T. Virus-like particle nanoreactors: programmed encapsulation of the thermostable CelB glycosidase inside the P22 capsid. *Soft Matter* **2012**, *8*, 10158–10166.
- (52) Kelly, P.; Anand, P.; Uvaydov, A.; Chakravartula, S.; Sherpa, C.; Pires, E.; O'Neil, A.; Douglas, T.; Holford, M. Developing a Dissociative Nanocontainer for Peptide Drug Delivery. *Int. J. Environ. Res. Public Health* **2015**, *12*, 12543–12555.
- (53) Lucon, J.; Edwards, E.; Qazi, S.; Uchida, M.; Douglas, T. Atom transfer radical polymerization on the interior of the P22 capsid and incorporation of photocatalytic monomer crosslinks. *Eur. Polym. J.* **2013**, *49*, 2976–2985.

- (54) Edwards, E.; Roychoudhury, R.; Schwarz, B.; Jordan, P.; Lisher, J.; Uchida, M.; Douglas, T. Co-localization of catalysts within a protein cage leads to efficient photochemical NADH and/or hydrogen production. *J. Mater. Chem. B* **2016**, *4*, 5375–5384.
- (55) King, J.; Lenk, E. V.; Botstein, D. Mechanism of Head Assembly and DNA Encapsulation in Salmonella Phage-P22 .2. Morphogenetic Pathway. *J. Mol. Biol.* 1973, 80, 697–731.
- (56) Hryc, C. F.; Chen, D. H.; Afonine, P. V.; Jakana, J.; Wang, Z.; Haase-Pettingell, C.; Jiang, W.; Adams, P. D.; King, J. A.; Schmid, M. F.; Chiu, W. Accurate model annotation of a near-atomic resolution cryo-EM map. *Proc. Natl. Acad. Sci. U.S.A.* **2017**, *114*, 3103–3108.
- (57) O'Neil, A.; Reichhardt, C.; Johnson, B.; Prevelige, P. E.; Douglas, T. Genetically programmed in vivo packaging of protein cargo and its controlled release from bacteriophage P22. *Angew. Chem., Int. Ed.* **2011**, *50*, 7425–7428.
- (58) Sharma, J.; Uchida, M.; Miettinen, H. M.; Douglas, T. Modular interior loading and exterior decoration of a virus-like particle. *Nanoscale* **2017**, 9, 10420–10430.
- (59) Zimmerman, S. B.; Trach, S. O. Estimation of Macromolecule Concentrations and Excluded Volume Effects for the Cytoplasm of *Escherichia Coli. J. Mol. Biol.* **1991**, 222, 599–620.
- (60) Uchida, M.; Flenniken, M. L.; Allen, M.; Willits, D. A.; Crowley, B. E.; Brumfield, S.; Willis, A. F.; Jackiw, L.; Jutila, M.; Young, M. J.; Douglas, T. Targeting of cancer cells with ferrimagnetic ferritin cage nanoparticles. *J. Am. Chem. Soc.* **2006**, *128*, 16626–16633.
- (61) Uchida, M.; Terashima, M.; Cunningham, C. H.; Suzuki, Y.; Willits, D. A.; Willis, A. F.; Yang, P. C.; Tsao, P. S.; McConnell, M. V.; Young, M. J.; Douglas, T. A Human Ferritin Iron Oxide Nanocomposite Magnetic Resonance Contrast Agent. *Magn. Reson. Med.* **2008**, *60*, 1073–1081.
- (62) Teschke, C. M.; McGough, A.; Thuman-Commike, P. A. Penton release from p22 heat-expanded capsids suggests importance of stabilizing penton-hexon interactions during capsid maturation. *Biophys. J.* 2003, 84, 2585–2592.
- (63) Prevelige, P. E., Jr.; Thomas, D.; King, J. Scaffolding protein regulates the polymerization of P22 coat subunits into icosahedral shells in vitro. *J. Mol. Biol.* **1988**, 202, 743–757.
- (64) Kang, S.; Uchida, M.; O'Neil, A.; Li, R.; Prevelige, P. E.; Douglas, T. Implementation of P22 Viral Capsids as Nanoplatforms. *Biomacromolecules* **2010**, *11*, 2804–2809.
- (65) Teschke, C. M.; King, J. Folding of the phage P22 coat protein in vitro. *Biochemistry* **1993**, 32, 10839–10847.
- (66) Fuller, M. T.; King, J. Purification of the Coat and Scaffolding Proteins from Procapsids of Bacteriophage P22. *Virology* **1981**, *112*, 529–547.
- (67) Schindelin, J.; Arganda-Carreras, I.; Frise, E.; Kaynig, V.; Longair, M.; Pietzsch, T.; Preibisch, S.; Rueden, C.; Saalfeld, S.; Schmid, B.; Tinevez, J. Y.; White, D. J.; Hartenstein, V.; Eliceiri, K.; Tomancak, P.; Cardona, A. Fiji: an open-source platform for biological-image analysis. *Nat. Methods* **2012**, *9*, 676–682.
- (68) Suloway, C.; Pulokas, J.; Fellmann, D.; Cheng, A.; Guerra, F.; Quispe, J.; Stagg, S.; Potter, C. S.; Carragher, B. Automated molecular microscopy: The new Leginon system. *J. Struct. Biol.* **2005**, *151*, 41–60
- (69) Suloway, C.; Shi, J.; Cheng, A.; Pulokas, J.; Carragher, B.; Potter, C. S.; Zheng, S. Q.; Agard, D. A.; Jensen, G. J. Fully automated, sequential tilt-series acquisition with Leginon. *J. Struct. Biol.* **2009**, *167*, 11–18.
- (70) Kremer, J. R.; Mastronarde, D. N.; McIntosh, J. R. Computer visualization of three-dimensional image data using IMOD. *J. Struct. Biol.* **1996**, *116*, 71–76.
- (71) Pettersen, E. F.; Goddard, T. D.; Huang, C. C.; Couch, G. S.; Greenblatt, D. M.; Meng, E. C.; Ferrin, T. E. UCSF chimera A visualization system for exploratory research and analysis. *J. Comput. Chem.* **2004**, *25*, 1605–1612.
- (72) Jordan, P. C.; Patterson, D. P.; Saboda, K. N.; Edwards, E. J.; Miettinen, H. M.; Basu, G.; Thielges, M. C.; Douglas, T. Self-

- assembling biomolecular catalysts for hydrogen production. *Nat. Chem.* **2016**, *8*, 179–185.
- (73) Sánchez-Sánchez, L.; Tapia-Moreno, A.; Juarez-Moreno, K.; Patterson, D. P.; Cadena-Nava, R. D.; Douglas, T.; Vazquez-Duhalt, R. Design of a VLP-nanovehicle for CYP450 enzymatic activity delivery. J. Nanobiotechnol. 2015, 13, No. 66.
- (74) Llauró, A.; Luque, D.; Edwards, E.; Trus, B. L.; Avera, J.; Reguera, D.; Douglas, T.; Pablo, P. J.; Caston, J. R. Cargo-shell and cargo-cargo couplings govern the mechanics of artificially loaded virus-derived cages. *Nanoscale* **2016**, *8*, 9328–9336.
- (75) Patterson, D. P.; Prevelige, P. E.; Douglas, T. Nanoreactors by programmed enzyme encapsulation inside the capsid of the bacteriophage P22. ACS Nano 2012, 6, 5000–5009.
- (76) Sun, J.; DuFort, C.; Daniel, M. C.; Murali, A.; Chen, C.; Gopinath, K.; Stein, B.; De, M.; Rotello, V. M.; Holzenburg, A.; Kao, C. C.; Dragnea, B. Core-controlled polymorphism in virus-like particles. *Proc. Natl. Acad. Sci. U.S.A.* **2007**, *104*, 1354–1359.
- (77) McCoy, K.; Selivanovitch, E.; Luque, D.; Lee, B.; Edwards, E.; Caston, J. R.; Douglas, T. Cargo Retention inside P22 Virus-Like Particles. *Biomacromolecules* **2018**, *19*, 3738–3746.
- (78) Levi, S.; Luzzago, A.; Cesareni, G.; Cozzi, A.; Franceschinelli, F.; Albertini, A.; Arosio, P. Mechanism of ferritin iron uptake: activity of the H-chain and deletion mapping of the ferro-oxidase site. A study of iron uptake and ferro-oxidase activity of human liver, recombinant H-chain ferritins, and of two H-chain deletion mutants. *J. Biol. Chem.* 1988, 263, 18086–18092.
- (79) Reichhardt, C.; Uchida, M.; O'Neil, A.; Li, R.; Prevelige, P. E.; Douglas, T. Templated assembly of organic-inorganic materials using the core shell structure of the P22 bacteriophage. *Chem. Commun.* **2011**, 47, 6326–6328.
- (80) Selivanovitch, E.; Koliyatt, R.; Douglas, T. Chemically Induced Morphogenesis of P22 Virus-like Particles by the Surfactant Sodium Dodecyl Sulfate. *Biomacromolecules* **2019**, *20*, 389–400.
- (81) Sharma, J.; Douglas, T. Tuning the catalytic properties of P22 nanoreactors through compositional control. *Nanoscale* **2020**, *12*, 336–346.
- (82) Ellis, R. J.; Minton, A. P. Cell biology Join the crowd. *Nature* **2003**, 425, 27–28.